The leading, interdecadal eigenmode of the Atlantic meridional overturning circulation in a realistic ocean model

Florian Sévellec*, Alexey V. Fedorov

Department of Geology and Geophysics, Yale University, New Haven, Connecticut, USA

Submitted to *Journal of Climate*, 06 January 2011

Revised, 04 August 2011

**Corresponding author address:* Department of Geology and Geophysics, Yale University, 210 Whitney Avenue, PO Box 208109, New Haven, CT 06520-8109, USA. Phone: 203-432-1959 – email: florian.sevellec@yale.edu

Abstract

Variations in the strength of the Atlantic meridional overturning circulation (AMOC) are a major potential source of decadal and longer climate variability in the Atlantic. In this study, we analyze continuous integrations of tangent linear and adjoint versions of an ocean General Circulation Model (OPA) and rigorously show the existence of a weakly-damped oscillatory eigenmode centered in the North Atlantic and controlled solely by linearized ocean dynamics. In this particular GCM the mode period is roughly 24 years, its e-folding decay timescale is 40 years, and the mode is the least damped in the system. Its mechanism is related to the westward propagation of temperature anomalies in the northern Atlantic in the latitudinal band between 30 and 60°N: these temperature anomalies modify density in the upper 1000 m of the ocean and hence, by geostrophic balance, ocean currents which then affect the temperature field. Salinity variations partially compensate the effect of temperature on density but, in general, have a smaller role in the oscillation (except during the excitation of the mode by initial perturbations). The westward propagation of temperature anomalies results from of a competition between mean eastward zonal advection, equivalent anomalous westward advection due to the mean meridional temperature gradient, and westward propagation typical of long baroclinic Rossby waves. When a temperature anomaly arrives at the basin western boundary, the ensuing geostrophic adjusment modifies the AMOC in about 2 years. Further, we show that the system is nonnormal, which implies that the structure of the eigenmode is different from the least-damped mode of the adjoint model. The latter mode describes the sensitivity of the system, *i.e.* which patterns, chosen as initial conditions, are most efficient for exciting the eigenmode. An idealized model is presented to highlight the role of the background meridional temperature gradient in the North Atlantic in the mechanism of the interdecadal mode and the nonnormality of the system.

1 Introduction

Variability of the Atlantic Meridional Overturning Circulation (AMOC) is believed to be a major source of climate variability in the Atlantic on timescales from decadal to centennial and longer. Observational, modeling and theoretical studies suggest a number of potential mechanisms and climate modes that can lead to temporal variations in the AMOC (for a recent review see Yoshimori et al., 2010). Similarly, comprehensive climate models show a broad diversity of the simulated AMOC variability - its amplitude, typical periods, and the possible mechanisms of the dominant climatic mode vary greatly from one model to the next (*e.g.* AR4, IPCC, 2007) and remain a subject of continuing debates. This work focuses on a robust interdecadal oscillatory mode (an eigenmode) that can exist in the system.

Many studies of climate variability in the Atlantic concentrate on the dynamics of the Atlantic Multidecadal Oscillation (AMO) – climate variability typically associated with periods between 50 to 70 yr (Kushnir, 1994; Delworth and Mann, 2000) and variations in the AMOC intensity of the order of several Sverdrups (Knight et al., 2005). The AMO can exert strong impacts on climate, affecting hurricane activity over the North Atlantic (Goldenberg et al., 2001) and precipitation over North America (Sutton and Hodson, 2005). Sutton and Hodson (2003) linked the climate change over the North Atlantic during the period 1871-1999 to the AMO.

AMO-like multidecadal variability has been studied in climate models of different complexity (Yoshimori et al., 2010; Latif, 1997). Several physical mechanisms for the AMO have been proposed, including changes in the subtropical gyre (Dong and Sutton, 2005; D'Orgeville and Peltier, 2009; Cheng et al., 2004) or changes in the subplolar gyre that alter the heat budget of the Labrador sea (Danabasoglu, 2008), just to give a few examples.

Recent observational studies show not only the existence of the 50-70 year variability, but also of variability in the 20-30 year band (Frankcombe et al., 2008). This shorter-period, interdecadal variability, can be identified by looking at temperature or sea level height (SLH)

variations in latitudinal bands (instead of using the average sea surface temperature over the North Atlantic - a classical AMO index). This interdecadal variability is characterized by a westward propagation of temperature anomaly. Analyzing zonal variations in SLH, Frankcombe and Dijkstra (2009) found such variability both in observations and climate models. The authors hypothesize that the AMO might have a strong signature at 20-30 years in addition to the 50-70 year band more commonly associated with the AMO. They point out, however, that the relatively short records analyzed in their study may have overemphasized shorter periods in the data.

Idealized ocean models also show that a westward propagating mode, acting on interdecadal time scale, can exist in the system. Several theories have been put forward to explain this mode: Huck et al. (1999) and Colin de Verdière and Huck (1999) suggest that this mode is associated with a large-scale Rossby wave propagating westward across the north-south thermal gradient. In contrast, te Raa and Dijkstra (2002) interpret the mode propagation as a result of interaction between the ocean stratification and an anomalous vertical flow induced by non-divergent geostrophic flow along the boundary. However, more recently te Raa et al. (2004) and Dijkstra et al. (2006) have shown that the mode does not change when an idealized rectangular basin is replaced with the realistic North Atlantic coastline.

Two recent studies suggest that this interdecadal mode can be sustained by atmospheric noise (Frankcombe et al., 2009; Sévellec et al., 2009), but they do not agree on the properties of the mode (whether the system is normal or nonnormal, *i.e.* the eigenmodes form an orthogonal or a non-orthogonal basis, *e.g.* Ioannou, 1995). Frankcombe et al. (2009) has proposed that the decadal timescale is a signature of a damped internal normal mode of the ocean; however, Sévellec et al. (2009) demonstrated the importance of the nonnormality for setting the amplitude of decadal variability (as discussed by Farrell and Ioannou, 1996, climate variability excited in a nonnormal system should be stronger than in an analogous normal system). In addition, a potential role of freshwater fluxes for the interdecadal mode

has been discussed, in idealized settings, by Chen and Ghil (1995) and more recently by te Raa and Dijkstra (2003) and Sévellec et al. (2009).

A fundamental question that has not been rigorously addressed yet is whether an interdecadal natural mode of oscillation controlled by ocean dynamics (an eigenmode rather than a mode of variability) would exist in realistic ocean conditions. This is the central question of the present study. Specially, using a tangent linear version of a realistic ocean GCM, we extract the least-damped eigenmode of the system and explore its underlying mechanisms and key properties. In our calculations the mode period is close to 24 years and the damping timescale to 40 years. We show that the westward propagation of temperature anomalies is critical for this mode and results from the competition between (i) the mean eastward zonal advection, (ii) the equivalent anomalous westward advection that depends on the mean meridional thermal gradient in the ocean, and (iii) the westward advection typical of long baroclinic Rossby waves (related to the β-effect).

Using the tangent linear and adjoint versions of this GCM and an idealized model, we also examine the role of nonnormality in ocean dynamics. We demonstrate that the structures of the least-damped mode of the forward model and of its adjoint (*i.e.* the biorthogonal mode) are drastically different. We also show that salinity anomalies and changes in the deep ocean play only a minor part in the oscillatory mechanism of the interdecadal mode; however, both effects can be important for exciting this mode via a transient nonnormal growth in the system.

The structure of the paper is as follows: In section 2, we will describe the ocean GCM and the methodology we use to obtain the least-damped eigenmodes of the tangent linear model and its adjoint. In section 3, we will discuss the properties of the eigenmode and the adjoint mode. In section 4, we will formulate an idealized model to further examine the properties of the oscillation. In section 5, we will summarize the implications of the study.

2 Methods

a. Ocean models and model configurations

In this study we use the ocean GCM OPA 8.2 (Océan PArallélisé, Madec et al., 1998) in its 2° global configuration (ORCA2, Madec and Imbard, 1996). There are 31 levels in the vertical - the level thickness varies from 10 m at the surface to 500 m at depth. The model is integrated using an Arakawa C-grid and the z-coordinates, and the rigid-lid approximation.

The present model configuration makes use of the following parameterizations: convection is parameterized by an increase in the vertical diffusion when the ocean vertical stratification is unstable; double diffusion is taken into account by two different terms for mixing temperature and salinity; eddy-induced velocities are described by the Gent and McWilliams (1990) approximation; the viscosity coefficient follows the turbulent closure scheme of Blanke and Delecluse (1993) and are functions of longitude, latitude and depth; and the mixing coefficient for temperature and salinity vary in longitude and latitude (Redi, 1982).

The tangent linear and adjoint models are provided by the OPATAM code (OPA Tangent Adjoint Model, Weaver et al., 2003), which is based on the linearization of the OPA's primitive equations of motions with respect to the ocean seasonally-varying basic state of the ocean.

For the present study, we impose surface heat and freshwater fluxes (from the model climatology) and do not use surface restoring. These fluxes are computed by running the full nonlinear model in a forced mode. This approach produces a realistic seasonal cycle for the linear and adjoint models, but reduces the damping and allows SST anomalies to develop more easily (Huck and Vallis, 2001; Arzel et al., 2006; Sévellec et al., 2009), for details see below.

Several additional approximations have been introduced for the tangent linear and adjoint models: the viscosity coefficients, the tracer mixing coefficients, and the eddy-induced ad-

vection, are calculated only for the basic ocean state - further variations in those coefficients are neglected.

b. Ocean basic state and linearization

The ocean basic state. The seasonally-varying basic state of the ocean, here also referred to as the annual model "trajectory", is obtained by a direct integration of the OPA model subject to the climatological surface boundary forcing (varying with the annual cycle). For the forcing, we use ECMWF heat fluxes averaged for the interval 1979 - 1993, the ERS wind stress blended with the TAO data between 1993 - 1996, and an estimate of the climatological river runoff. In addition, we apply a surface temperature restoring to the Reynolds climatological SSTs averaged from 1982 to 1989, together with a surface salinity restoring to the Levitus (1989) climatology. A restoring term to the Levitus climatological values of temperature and salinity is applied in the Red and Mediterranean Seas (we emphasize that no restoring is used in the linear models). Starting with the Levitus climatology as the initial conditions, the model produces a quasi-stationary annual cycle of the ocean basic state after 200 years of integration.

The Atlantic meridional overturning circulation (AMOC) in the full GCM (Fig. 1) is characterized by the northward mass transport above the thermocline, a southward return flow between 1500-3000 m, and a recirculation cell below 3000 m associated with the Antarctic Bottom Water. The maximum volume transport of the AMOC is around 14 Sv, which is slightly below but still within the errorbars of the observations (18±5 Sv, Talley et al., 2003). The AMOC poleward heat transport reaches 0.8 PW at 25°N, whereas estimations from inverse calculations and hydrographic sections give 1.3 PW at 24°N (Ganachaud and Wunsch, 2000).

As expected, the SST field develops a strong meridional gradient in the northern Atlantic, especially across the North Atlantic Current (NAC), and a salinity maximum at about 20°N

(Fig. 1). The barotropic streamfunction shows an intense subtropical gyre and a weaker subpolar gyre centered at about 60°N. The two gyres are separated by the NAC.

Overall, the full nonlinear model produces a realistic (seasonally-varying) basic state of the ocean. Next, we will conduct a linear stability analysis of this ocean state.

Linear experiments. The goal of these experiments is to identify the least-damped eigenmodes of the tangent linear and adjoint models (linearized with respect to the seasonally varying basic state) by condicting long continuous integrations and applying a Poincaré section (Strogatz, 1994). Alternatively, we could use the Floquet theorem and transform the periodic system to a traditional linear system with constant coefficients. However, in our case, obtaining the eigenmodes requires the diagonalization of a matrix of the size 3,400,011×3,400,011. This task goes beyond the limits of our computational capabilities; consequently, we apply a different approach.

A non-autonomous dynamical system, such as that of a GCM, can be written as

$$d_t \left|\boldsymbol{U}\right\rangle = \mathcal{N}\left(\left|\boldsymbol{U}\right\rangle, t\right), \tag{1}$$

where t is time, $|\boldsymbol{U}\rangle$ - the state vector of all prognostic variables and $\mathcal{N}$ - a time-dependent nonlinear operator. We also define the notation $\langle\boldsymbol{U}|$ through the Euclidian norm $\langle\boldsymbol{U}|\boldsymbol{U}\rangle$, defined through the scalar product (often called the dot product). After we decompose the state vector as $|\boldsymbol{U}\rangle=|\bar{\boldsymbol{U}}\rangle+|\boldsymbol{u}\rangle$, where $|\bar{\boldsymbol{U}}\rangle$ is the nonlinear annual trajectory and $|\boldsymbol{u}\rangle$ is a perturbation, the time evolution of the perturbation can be described by a linear equation

$$d_t \left|\boldsymbol{u}\right\rangle = \left.\frac{\partial \mathcal{N}}{\partial \left|\boldsymbol{u}\right\rangle}\right|_{|\bar{\boldsymbol{U}}\rangle} \tag{2}$$

We rewrite this latter equation using a non-autonomous propagator $\mathbf{M}$ that connects perturbations at time t_1 to those at time t_2 as:

$$\left|\boldsymbol{u}(t_2)\right\rangle = \mathbf{M}\left(t_2, t_1\right)\left|\boldsymbol{u}(t_1)\right\rangle \tag{3}$$

In a discretized system $\mathbf{M}$ is a matrix.

Further, we can simplify (3) by eliminating the seasonal cycle from consideration and using the first recurrence map analysis (also called a Poincaré section). This procedure removes one codimension, allowing us to study the stability of a fixed point instead of a limit cycle (Strogatz, 1994). Specifically, we extract from the matrix $\mathbf{M}$ all points that occur at the same time of the seasonal cycle every year (Δt=1 yr) – for example, the points that occur on the 31$^{\text{th}}$ December (t^*). Because the only time dependency in the linearized operator comes from the climatological seasonal cycle, by this procedure, we obtain a new autonomous dynamical system (denotes by $\tilde{}$).

$$\tilde{\mathbf{M}}\left(t = n\Delta t\right) = \mathbf{M}\left(t^* + n\Delta t, t^*\right), \tag{4}$$

where n and t are integers representing the number of seasonal cycle number and the new time, respectively.

The linear and adjoint models of this system can be rewritten in term of their eigenvectors as:

$$\tilde{\mathbf{M}}(t) = \sum_j |\boldsymbol{u}_j\rangle\, e^{\lambda_j t}\, \langle \boldsymbol{u}_j^\dagger|\,, \tag{5a}$$

$$\tilde{\mathbf{M}}^\dagger(t) = \sum_j |\boldsymbol{u}_j^\dagger\rangle\, e^{\lambda_j^* t}\, \langle \boldsymbol{u}_j|\,, \tag{5b}$$

where $\tilde{\mathbf{M}}^\dagger$ the adjoint propagator matrix (defined through the Euclidian norm), $|\boldsymbol{u}_j^{(\dagger)}\rangle$ and $\lambda_j^{(*)}$ are the eigenvectors and eigenvalues of $\tilde{\mathbf{M}}^{(\dagger)}$ (where * denotes the complex conjugate), and the sum over j represents summation over all eigenvectors (corresponding to the number of degrees of freedom in the discretized model).

Because e-folding decay scales of the eigenmodes differ from each other ($1/\Re(\lambda_j)$, where $\Re$ denotes the real part), on long time scales (t$\rightarrow\infty$) only the least-damped eigenmode will persist: that is, the eigenmode with the minimum value of $\Re(\lambda_j)$. We will denote this mode

by index j=1. Then, the tangent linear and adjoint models yield:

$$\lim_{t\to\infty} \tilde{\mathbf{M}}(t) = \lim_{t\to\infty} |\boldsymbol{u}_1\rangle\, e^{\lambda_1 t}\, \langle \boldsymbol{u}_1^\dagger|\,, \tag{6a}$$

$$\lim_{t\to\infty} \tilde{\mathbf{M}}^\dagger(t) = \lim_{t\to\infty} |\boldsymbol{u}_1^\dagger\rangle\, e^{\lambda_1^* t}\, \langle \boldsymbol{u}_1|\,, \tag{6b}$$

Thus, if $|\boldsymbol{u}(0)\rangle$ is an arbitrary initial condition, on long time scale the outputs, $|\boldsymbol{u}(t)\rangle$, of the tangent linear and adjoint models are controlled by their least-damped eigenmodes:

$$|\boldsymbol{u}(\infty)\rangle = \lim_{t\to\infty} \tilde{\mathbf{M}}(t)\,|\boldsymbol{u}(0)\rangle = \lim_{t\to\infty} |\boldsymbol{u}_1\rangle\, e^{\lambda_1 t}\, \langle \boldsymbol{u}_1^\dagger|\boldsymbol{u}(0)\rangle \propto |\boldsymbol{u}_1\rangle\,, \tag{7a}$$

$$|\boldsymbol{u}(\infty)\rangle = \lim_{t\to\infty} \tilde{\mathbf{M}}^\dagger(t)\,|\boldsymbol{u}(0)\rangle = \lim_{t\to\infty} |\boldsymbol{u}_1^\dagger\rangle\, e^{\lambda_1^* t}\, \langle \boldsymbol{u}_1|\boldsymbol{u}(0)\rangle \propto |\boldsymbol{u}_1^\dagger\rangle\,, \tag{7b}$$

Accordingly, to obtain the least-damped eigenmodes for these two cases, we have conducted several long-time integrations of the tangent linear model and its adjoint, with durations exceeding 500 yr. For the forward model we used four different initial conditions, $|\boldsymbol{u}(0)\rangle$, to check the convergence of the asymptotic output, $|\boldsymbol{u}(\infty)\rangle$, to the same eigenvector $|\boldsymbol{u}_1\rangle$. For the adjoint model we used three different initial conditions to check the convergence to $|\boldsymbol{u}_1^\dagger\rangle$. Note that in the latter case, the integration was conducted from the initial conditions but backward in time.

3 Results

a. The least-damped linear mode of the system

Analyzing the output of the tangent linear model reveals the existence in the system of a damped oscillatory eigenmode centered in the North Atlantic with a period of about 24 yr and an e-folding decay time scale of 40 yr (Fig. 2). This interdecadal mode exhibits a nearly quadrature phase relationship between variations in the AMOC strength and the upper ocean temperature averaged over the northern Atlantic (Fig. 2, top). The heat content of the Labrador sea appears to be a good precursor, by roughly 2 yr, of the AMOC changes (Fig. 2, bottom). Similar phased changes in the ocean heat content, the Labrador sea

heat content, and the AMOC transport on multidecadal timescales have been discussed by Danabasoglu (2008).

Temperature variations associated with the interdecadal mode in our model are most pronounced in the upper 500 m of the northern Atlantic Ocean between 30°N and 60°N (Fig. 3, top). The temporal evolution of the mode exhibits two distinct (quadrature) phases – phases A and B (Fig. 2, top). Phase (A) is characterized by a strong anomaly of the zonally-averaged temperature in the upper ocean but almost no anomaly in the ocean large-scale meridional overturning, whereas phase (B) has very weak anomaly in zonally-averaged temperature but a strong anomaly in the overturning streamfunction (Fig. 3).

During the first phase of the oscillation (A), a cooling of the upper ocean induces anomalous horizontal velocity around the temperature or, more accurately, density anomaly (Fig. 3, top left). The anomalous geostrophic flow (cyclonic for a cold anomaly) modifies both the subtropical and subpolar gyre circulation. In the upper ocean, this flow acts on the background meridional temperature gradient, bringing warm waters from the South into eastern part of the basin and cold waters from the North into the western part. This mechanism, together with the β-effect, effectively leads to the westward propagation of the initial temperature anomaly. At depth, in the absence of a mean temperature gradient comparable to that in the upper ocean, the anomalous velocity has little effect on temperature changes. Also, since the anomalous circulation occurs around a temperature anomaly of the same sign (versus a dipole), the southward and northward velocities largely compensate each other and contribute little to the meridional overturning (Fig. 3, bottom left).

The westward propagation of the cold temperature anomaly and the anomalous flow from the South causes the development of a new, warm temperature anomaly on the right flank of the initial anomaly (Fig. 5). This dipole pattern of temperature (cold-warm) becomes most pronounced by the second phase of the oscillation (phase B in Fig. 3, right panels). In turn, the zonal temperature gradient within the temperature dipole generates a northward

geostrophic velocity anomaly in the upper ocean and a positive anomaly in the meridional overturning. The westward propagation of alternating temperature anomalies is evident from the Hovmoller diagrams for the mode with the amplitude decay suppressed (Fig. 6).

In the discussion above, we have implicitly assumed that the background meridional density gradient is controlled by temperature ($|\alpha\partial_y\overline{T}|\gg|\beta\partial_y\overline{S}|$). This assumption holds fairly well in the Atlantic north of 30°N (Fig. 7). Therefore, anomalous meridional velocity in this region acts mostly on the mean temperature rather than salinity gradient when generating density anomalies. That is why, the dynamics of the mode are predominantly controlled by temperature variations.

Nevertheless, the oscillatory mode does have a salinity component (Fig. 4). Even though temperature and salinity anomalies have similar shapes and propagation characteristics, salinity anomalies act to reduce the effect of temperature anomalies on density (*c.f.* Figs. 3 and 4). This behavior is a consequence of the opposite effects on density of the mean meridional gradients of temperature and salinity. That is, anomalous northward advection extracts from the mean fields positive anomalies in temperature and salinity. The latter partially compensates the effect of the former on density. In simplified models such compensation has been discussed by Huck et al. (1999), Huck and Vallis (2001), te Raa and Dijkstra (2002), and Sévellec et al. (2009).

We should also emphasize that the eigenmode we describe is not driven by convection. In fact, the approximations of the tangent linear and adjoint models assume that tracer diffusivities are fixed, and so is the ocean mixed layer depth. Consequently all changes in the vertical flow are determined by divergence or convergence of the horizontal flow associated with large-scale density anomalies. Thus, our results confirm that AMOC variability can occur without changes in the mixed layer depth and hence convection. This is not to say, however, that this mode will not influence deep convection, but rather changes in convection will be a next-order effect for the dynamics.

b. The biorthogonal mode

Using a similar mathematical procedure we have computed the least-damped eigenmodes ($|\boldsymbol{u}_1^\dagger\rangle$) of the propagator of the adjoint model ($\tilde{\mathbf{M}}^\dagger$). This mode is defined as the biorthogonal to the least-damped eigenmode of the tangent linear propagator ($|\boldsymbol{u}_1\rangle$). That is, the biorthogonal mode is orthogonal to every eigenmode of the tangent linear propagator except $|\boldsymbol{u}_1\rangle$ (defining the contravariant projection). If the system is nonnormal ($\tilde{\mathbf{M}}\tilde{\mathbf{M}}^\dagger$–$\tilde{\mathbf{M}}^\dagger\tilde{\mathbf{M}}\neq 0$), the least-damped mode of the tangent linear model and that of the adjoint will differ from each other ($|\boldsymbol{u}_1\rangle\neq|\boldsymbol{u}_1^\dagger\rangle$). Because of this nonnormality we can expect a stronger temporal variability in the system (Ioannou, 1995) associated with the efficient stimulation of the eigenmodes of the tangent linear model that occurs through the stimulation of their biorthogonals. This stems from the fact that $|\boldsymbol{u}_1^\dagger\rangle$ has the biggest normalized covariant projection on $|\boldsymbol{u}_1\rangle$.

As expected, the least-damped mode of the adjoint has the same period and decay scale as that of the tangent linear model. However, the spatial structure of the adjoint mode is very different. For instance, temperature and salinity anomalies in the adjoint mode have a constructive effect on density, rather than compensating as in the tangent linear mode (also discussed previously in a simplified model by Sévellec et al., 2009). The effect of salinity on density in the adjoint mode slightly dominates that of temperature. The adjoint mode is most pronounced in the deep ocean below 500 m north-west of the North Atlantic Current. (Figs. 8 and 9).

As mentioned before, since they are biorthogonal to each other, the least-damped mode of the adjoint has the maximum covariant projection onto the least-damped mode of the tangent linear model. Consequently, the former controls the sensitivity of the latter to initial perturbations. Thus, to understand the spatial structure of the biorthogonal mode, it is important to understand why specific changes in temperature or salinity in a particular region can stimulate efficiently the leading eigenmode of the tangent linear model. In our case, temperature and salinity anomalies of the biorthogonal mode are located predominantly

in the area where they can avoid propagation or deformation, which allows them to impact the ocean circulation most efficiently.

In fact, temperature and salinity anomalies of the biorthogonal mode are strongest in the region where ocean currents are weak (away from the NAC, Fig. 11, left) and at depths where horizontal density gradients vanish and so does the possibility for westward propagation. Such anomalies are able to create a persistent anomalous advection, through thermal wind balance, and hence stimulate the least-damped mode of the tangent linear model. The fact that the speed of propagation of temperature and salinity anomalies in the biorthogonal mode is very slow allows an efficient excitation of the interdecadal mode on long time scales, which principally explains the overall structure of the biorthogonal mode.

The constructive effect of temperature and salinity on density in the biorthogonal mode can be understood by the same logic. A constructive density anomaly will induce a greater anomalous velocity which will be more efficient in extracting temperature anomalies from the background temperature field, and thus more efficient in generating the least-damped mode of the tangent linear (forward) model.

To summarize, the stimulation of the eigenmode by its biorthogonal can be described by the following process: together, temperature and salinity anomalies of the biothothogonal pattern induce a strong geostrophic flow. In turn, this flow extracts from the mean ocean state new anomalies in temperature and salinity. The new anomalies have opposite effects on density, but since the ocean mean state is dominated by the meridional temperature gradient, density anomalies are now controlled largely by temperature. These density anomalies propagate westward and define the oscillatory eigenmode dominated by temperature and partially compensated by salinity.

4 The idealized model

a. Formulation

To better understand the oscillatory mechanism of the mode in the ocean GCM we have formulated an idealized model that includes the essential linear dynamics of the oscillation and westward propagation.

The idealized model has only two levels in the vertical (Fig. 10) and invokes several key approximations. For simplicity, given the decadal time scale of the oscillation, we consider the system as autonomous (no seasonal cycle). Also, the large, basin scale of the mode allows us to reduce the momemtum equations to the geostrophic balance on a β-plane (*i.e.* the planetary-geostrophic regime, Colin de Verdière, 1988).

Given the dominant effect of temperature on density in the mode ($|\beta S'| \ll |\alpha T'|$, where T' and S' are temperature and salinity anomalies, respectively), at first we restrict the dynamics to temperature variations. Accordingly, the model describes anomalies in temperature at two levels - the top level (of depth h) and the deep level. We define the upper ocean as the part of the ocean with a strong stratification, and the deep ocean - with weak or no stratification. To simplify the mathematical procedure of the analysis, meridional variations in T' are neglected (anomalies are considered to be functions of time t and the zonal coordinate x). The zonal extent of the model ocean is W; the full ocean depth is H.

In the absence of stratification at the deep level, we choose T' - temperature anomalies in the upper ocean - as prognostic variables of the model (for simplicity we drop the indices of Fig. 10, in the rest of this section). They evolve according to a linearized advective-diffusion equations with horizontal diffusivity κ:

$$\partial_t T' = \overline{u}\partial_x T' + v'\partial_x \overline{T} + w'\partial_z \overline{T} + \partial_x \left(\kappa \partial_x T'\right), \tag{8}$$

where v' and w' are anomalous meridional and vertical velocities, respectively.

This equation is linearized with respect to the mean state of the ocean. In particular,

in the upper level we impose a mean zonal flow, $\overline{u}$, and mean temperature gradient. This gradient has meridional and vertical components: $\partial_y \overline{T}$, and $\partial_z \overline{T}$, where y and z are the meridional and vertical coordinates, and $\overline{T}$ is the mean temperature. The mean zonal gradient of temperature is neglected. The values of the mean fields in (8) are given by simple constants estimated from the climatologycal run with the ocean GCM.

The system is closed using a linear equation of state for seawater, thermal wind balance for the meridional velocity with the baroclinicity condition, and the condition of non-divergence for the anomalous flow.

$$\partial_z v' = \frac{\alpha g}{f} \partial_x T' \text{ with } \int_{-H}^{0} dz\, v' = 0, \tag{9a}$$

$$\partial_y v' + \partial_z w' = 0, \text{ with } w'|_{z=0} = 0, \tag{9b}$$

where f is the Coriolis parameter, g - the acceleration of gravity, α - the haline contraction coefficient (for the typical values of these parameters see Tab 1).

Using thermal wind balance, the baroclinicity condition, and considering ocean dynamics at the top and deep levels, we obtain a simple expression for the anomalous meridional velocity in the upper ocean:

$$v' = \frac{\alpha g \tilde{h}}{f} \partial_x T'. \tag{10}$$

where $\tilde{h}=(H-h)/2$. The divergence of this meridional flow will induce anomalous vertical velocity

$$w' = \frac{\alpha g \tilde{h} h}{f^2} \beta_f \partial_x T', \tag{11}$$

where $\beta_f=\partial_y f$ is the meridional gradient of planetary vorticity.

Using (8), (10), and (11), we reduce the dynamics of the idealized model at the upper level to one equation:

$$\partial_t T' = -c \partial_x T' + \kappa \partial_{xx} T', \tag{12}$$

where

$$c = \overline{u} + \hat{u} + c_{\mathrm{Ro}}, \tag{13}$$

is the full speed of the mode propagation, with $\hat{u}=(\alpha g\tilde{h}/f)\partial_y\overline{T}$ and $c_{\rm Ro}=(\alpha g\tilde{h}h\beta_f/f^2)\partial_z\overline{T}$. Here $\hat{u}$ is the equivalent speed of westward propagation of temperature anomalies on the background meridional temperature gradient (geostrophic self-advection, as sketched in Fig. 5). $c_{\rm Ro}$ represents the phase velocity of long (non-dispersive) baroclinic Rossby waves due to the β-effect, and $\overline{u}$ described the mean eastward flow. Simple estimates show that the Rossby wave propagation speed is significantly slower than the geostrophic self-advection ($c_{\rm Ro}<\hat{u}$) in mid- to high latitudes.

Also, using the baroclinicity condition and the equation for v' in the upper ocean, we can compute variations in the meridional volume transport associated with temperature anomalies as

$$\psi' = \int_{-h}^{0}\int_{0}^{W} v' dx dz = (hW)\, V' = \frac{\alpha g\tilde{h}h}{f}\left(T'_W - T'_E\right), \tag{14}$$

Where ψ' is the anomalous transport, V' - the zonally-averaged meridional velocity, and T'_W and T'_E are temperature variations at the western and eastern boundaries of the basin, respectively. We will use this equation in the next sections.

Further, we expand temperature anomaly, T', into Fourier harmonics:

$$T' = \sum_n T_{cn}\cos\left(\frac{n\pi}{W}x\right) + T_{sn}\sin\left(\frac{n\pi}{W}x\right),$$

where n is the wave number. The Fourier amplitudes T_{cn} and T_{sn} obey simple differential equations:

$$\partial_t T_{cn} = c\frac{n\pi}{W}T_{sn} - \kappa\left(\frac{n\pi}{W}\right)^2 T_{cn}, \tag{15a}$$

$$\partial_t T_{sn} = -c\frac{n\pi}{W}T_{cn} - \kappa\left(\frac{n\pi}{W}\right)^2 T_{sn}, \tag{15b}$$

This system's complex conjugate eigenvalues are

$$\lambda_n^{\pm} = \lambda_{nr} \pm i\lambda_{ni} = -\kappa\left(\frac{n\pi}{W}\right)^2 \pm i\frac{n\pi}{W}c. \tag{16}$$

An estimate using ocean typical values from Tab. 1 gives for the gravest mode (with n=1) a period of $T=2\pi/\lambda_{1i}$=8.9 yr and an e-folding decay time scale of $\tau=1/\lambda_{1r}$=–36.1 yr. The

corresponding eigenvectors are:

$$|\boldsymbol{u}_n^{\pm}\rangle = \frac{\sqrt{2}}{2}\begin{pmatrix} \pm i \\ \\ 1 \end{pmatrix}.$$

We will demonstrate in the next sections that the relatively short period given by (16) becomes significantly longer and comparable to that in the ocean GCM if the effect of the meridional salinity gradient on density is taken into account.

b. The mode oscillatory mechanism and nonnormality

The idealized model and its eigenvectors confirm that the system can exhibit a damped oscillation in which temperature anomalies propagate westward (as long as the meridional gradient of temperature is strong enough to maintain the westward propagation tendency against the mean flow). The oscillation goes through two quadrature phases (corresponding to cosine and sine in the expression for T'). The first phase is characterized by an anomaly in the zonally-averaged temperature (proportional to the sine with n=1) and no change in meridional streamfunction (14), whereas the second phase is characterized by an anomaly in the zonal temperature gradient (proportional to the cosine with n=1) and a corresponding anomaly in the meridional overturning (14). Thus, the oscillation undergoes exactly the same phases as the least-damped mode of the tangent linear GCM – the phases characterized by variations in the zonally-averaged temperature followed by variations in the AMOC (as in Fig. 2).

Note that in more idealized settings, where both the mean flow and its perturbations are described solely by the first vertical baroclinic mode, as in the 1.5-layer shallow-water equations, the geostrophic self-advection of temperature anomalies and advection by the mean flow cancel each other, resulting in a westward propagation controlled exclusively by the β-effect. This cancellation is known as the non-Doppler effect (Rossby et al., 1939; Held, 1983; Killworth et al., 1997).

The role of wavenumber. According to expression (16), both the oscillation period and the e-folding decay timescale of different modes in the idealized model depend on wavenumber. In fact, the period is given by the inverse of wavenumber, while the e-folding decay timescale is given by the inverse of wavenumber squared. Therefore, modes with $n \geq 2$ are stronger damped by dissipative processes than the first mode (with $n=1$). This explains why the mode with the smallest wave number is the least-damped mode of the system.

The role of mean zonal velocity. To evaluate the importance of the mean eastward advection ($\overline{u}$), we can compare it to the equivalent zonal velocity due to the mean meridional temperature gradient, $\hat{u}=\alpha g \tilde{h} \partial_y \overline{T}/f$ This equivalent zonal velocity is westward as long as temperature decreases with latitude, and simple estimates (using parameters from Tab. 1) show that its magnitude far exceeds the eastward tendency of the mean zonal flow (Fig 11). The β-effect increases the westward tendency even further. Thus, temperature anomalies will indeed propagate westward in accordance with the mechanism described in Fig. 5 (also see Tab. 2), *i.e.* the geostrophic self-advection due to the background meridional temperature gradient. This gradient is strongest in the northern Atlantic, between 30 and 60°N, which tentatively explains the predominant location of the least-damped mode. Although the mean eastward advection is not needed for the oscillatory mechanism, it is still important in computing the period of the mode accurately (Fig. 12) as described in the next sections.

The role of the deep ocean: Other important effects, not critical for the existence of the mode but affecting its period and nonnormal dynamics, include salinity and the effect of the deep ocean. For example, as we showed in section 3b, the biorthogonal to the least-damped oscillatory mode of the linearized GCM has a stronger signature below 1000 m than at the surface (Fig. 8 and 9, section 3b).

To include the effect of the deep ocean, we need to modify the previous equations of idealized model – eqs (15). This can be done by adding to the system two new equations for

the Fourier amplitudes of the deep ocean temperature T^d_{cn} and T^d_{sn} (Appendix A). A linear stability analysis of the new system yields four eigenvalues:

$$\lambda_{1,2} = -\kappa \left(\frac{n\pi}{W}\right)^2 \pm i\frac{n\pi}{W}c, \quad \text{and} \quad \lambda_{3,4} = -\kappa \left(\frac{n\pi}{W}\right)^2, \tag{17}$$

where still $c{=}\overline{u}{+}\hat{u}{+}c_{\rm Ro}$, with $\hat{u}{=}\frac{\alpha g\tilde{h}}{f}\partial_y\overline{T}$ and $c_{\rm Ro}{=}\frac{\alpha g\tilde{h}h\beta_f}{f^2}\partial_z\overline{T}$.

The first two (oscillatory) eigenvalues of the system ($\lambda_{1,2}$) have not changed and the last two components of the corresponding eigenvectors are zero, so that in agreement with the tangent linear GCM (Figs. 3 and 4) the deep ocean does not directly affect the leading mode of the system.

The new eigenvalues ($\lambda_{3,4}$) are degenerate and describe a purely decaying mode with an e-folding decay timescale of approximately 36 yr. This mode also has a strong signature in the upper ocean.

We can examine the sensitivity of the eigenvectors (*i.e.* the best way to excite them) by computing their biorthogonals, see (22) in Appendix A. It turns out that, although the dynamics of the two damped modes $|\boldsymbol{u}_3\rangle$ and $|\boldsymbol{u}_4\rangle$ are mainly controlled by the upper ocean, their sensitivity, $|\boldsymbol{u}_3^\dagger\rangle$ and $|\boldsymbol{u}_4^\dagger\rangle$, are controlled solely by the deep ocean. The sensitivity of the oscillatory mode, $|\boldsymbol{u}_{1,2}^\dagger\rangle$, is also largely controlled by the deep ocean. Such asymmetry between the eigenvectors and their biothorgonals is a consequence of the nonnormality of the system dynamics.

These results are consistent with the analysis of the ocean GCM (section 3). That is, the deep ocean is a critical region for the sensitivity of the oscillatory mode, even though the mode itself manifest in the upper ocean. This is because temperature anomalies can persist longer in the deep ocean (where both mean currents and geostrophic self-advection are weak), and excite the oscillatory mode more efficiently.

The role of the salinity: Another important factor that can influence the properties of the leading oscillatory eigenmode and its sensitivity involves salinity variations. Using the

tangent linear GCM and its adjoint (section 3), we have shown that the oscillation dynamics are largely controlled by temperature variations in the upper ocean (with salinity having a compensating effect on density). However, the sensitivity of the oscillation, *i.e.* the biorthogonal mode, is controlled more or less equally by temperature and salinity (with the two having a constructive effect on density). These results are related again to the nonnormality of the system associated with the different effects on density of the mean temperature and salinity gradients in the northern Atlantic.

Here, we examine these results by extending the idealized model described by (15) to include salinity variations (but not the effect of the deep ocean). To that end, we introduce S_{cn} and S_{sn} - the Fourier amplitudes for the upper-ocean salinity (similar to T_{cn} and T_{cn}), which will add two more equations to system (15), for details see Appendix B.

A linear stability analysis of the new equations yields four eigenvalues:

$$\lambda_{1,2} = -\kappa \left(\frac{n\pi}{W}\right)^2 \pm i\frac{n\pi}{W}c, \text{ and } \lambda_{3,4} = -\kappa \left(\frac{n\pi}{W}\right)^2 \pm i\frac{n\pi}{W}\overline{u}, \tag{18}$$

where c=$\overline{u}$+$\hat{u}$+c_{Ro}, but now $\hat{u}$=$\left(\alpha\partial_y\overline{T} - \beta\partial_y\overline{S}\right) g\tilde{h}/f$ and c_{Ro}=$\left(\alpha\partial_z\overline{T} - \beta\partial_z\overline{S}\right) g\tilde{h}h\beta_f/f^2$.

The first two eigenvalues $\lambda_{1,2}$ and the corresponding eigenvectors are similar to those in the temperature-only model, but now the speed of westward propagation should be modified to include mean salinity variations. The oscillation is still dominated by temperature and the mode dynamics are described by the westward propagation of density anomalies as long as $|\alpha\partial_y\overline{T}|>|\beta\partial_y\overline{S}|$, which holds well in the northern Atlantic (Fig 11). However, the speed of westward geostrophic self-advection decreases because of the reduction of the mean meridional density gradient caused by salinity. Note that in the absence of the mean meridional temperature gradient the propagation of density anomalies would be eastward.

Estimating the period and the e-folding decay timescale of the leading oscillatory mode for the typical parameters in Tab. 1 and n=1 gives $2\pi/\Im(\lambda_{1,2})$=22.4 yr for the period and $1/\Re(\lambda_{1,2})$=–36 yr for the decay scale, which agrees well with the ocean GCM results.

The other two eigenvalues ($\lambda_{3,4}$) and the corresponding eigenvectors represent a mode

passively advected by the mean currents and damped by diffusion. It is a spiciness mode with eastward propagation (a spiciness anomaly does not modify density and hence cannot experience geostrophic self-advection). The period of this mode is 12 yr for the mean current of 2.5 cm s^{-1}, and its decay timescale is –36 yr.

As previously, differences between the mode dynamics and its sensitivity become apparent when we compare the eigenmodes and their biorthogonals (26a). The biorthogonals show that the passively-advected mode, $|\boldsymbol{u}_{3,4}\rangle$, is more sensitive to salinity than to temperature variations, even though the mode itself does not have any preferences between the two fields in its dynamics (since it is a spiciness mode). For the oscillatory mode, $|\boldsymbol{u}_{1,2}\rangle$, the biothogonals produce a constructive pattern of temperature and salinity without a dominant term, even though the eigenmode itself is controlled by temperature anomalies partially compensated by salinity. These results are similar to the GCM analysis (section 3), which again highlights that the ocean dynamics are nonnormal. The cause of nonnormality is the asymmetry between mean temperature and salinity fields.

c. The mode oscillation period

We can now return to the question of what controls the period of the interdecadal mode. Ultimately, this period is inversely proportional to c and thus proportional to the time needed for a temperature (or density) anomaly to cross the northern Atlantic. Our study points to several key factors that determine this crossing time, including the meridional gradients of temperature and salinity, the mean zonal velocity, and the width of the basin (the latter parameter, along with horizontal diffusivity, also controls the mode decay timescale). As previously discussed, the meridional salinity gradient and the mean zonal flow, although not critical for the oscillation, are indeed important for setting the period of the mode. By slowing down the westward propagation, these two factors lengthens the oscillation period (Tab. 2).

To further understand the sensitivity of the period to different processes in the idealized model, we varied four parameters in (18): the mean zonal velocity (from 0 to 0.1 m s^{-1}), the meridional temperature contrast (from –30 to 0 K), the prevailing latitude at which temperature anomalies propagate (from 20 to 80°N), and the ocean upper layer thickness (from 200 to 2000 m).

Analyzing the sensitivity of the mode to the mean zonal velocity and the meridional temperature gradient reveals two different regimes (Fig. 12, left panel) - with westward or eastward propagation. Which regime is achieved depends on whether the eastward flow is strong enough to overcome the westward tendency of the geostrophic self-advection and the β-effect. At the border between the two regimes the mode period goes to infinity (which corresponds to a zero propagation speed) and the oscillation degenerates into a purely damped, trapped mode.

The oscillation period also changes when the upper level thickness, h in (18), is modified. Increasing this thickness in the idealized model leads to a slower westward propagation speed and longer periods (before the direction of propagation changes sign), see Fig. 12, right panel. A similar effect occurs when we increase the prevailing latitude at which density anomalies propagate (which affects both the Coriolis and β parameters).

Varying the characteristic speed of the mean current also shows two different regimes (Fig. 12, left panel). For a fixed mean eastward flow, the eastward propagation of density anomalies becomes possible only in high latitudes and for a large thickness of the upper layer.

5 Conclusion

Ocean circulation can generate climate variability on a variety of timescales. In this study, we have conducted a stability analysis of a linearized version of a realistic ocean GCM and its adjoint and identified the leading (least damped), interdecadal eigenmode of the Atlantic

meridional overturning circulation. The mode is associated with large-scale westward propagating density anomalies dominated by temperature but partially compensated by salinity. These temperature anomalies are most pronounced in the upper ocean in the northern Atlantic in the band between 30 and 60°N where the mean meridional gradient of temperature is especially strong. In our particular model the least-damped mode has a period of 24 yr and an e-folding decay timescale of roughly 40 yr. The damping becomes stronger if the surface mixed boundary conditions are applied instead of the flux boundary conditions.

The westward propagation of temperature anomalies is largely explained by the geostrophic self-advection of the anomalies on the background of the mean meridional temperature gradient. Two other factors determining the propagation characteristics are the β-effect (as in conventional Rossby waves) and the mean eastward flow. Since the meridional salinity gradient in the North Atlantic mainly opposes that in temperature, the effect of salinity is to slow down the westward propagation. In general, the propagating temperature anomalies can be interpreted as planetary waves associated with the background vorticity gradient (controlled by variations in density and planetary vorticity) and affected by mean currents. The period of the mode is determined by the time necessary for the temperature anomalies to cross the northern Atlantic twice.

An idealized two-level model, based on planetary-geostrophic equations for temperature and salinity anomalies (e.g. Colin de Verdière, 1988), captures the main properties of the mode and emphasizes the importance of the mean meridional temperature gradient in the upper ocean for the mode dynamics. The meridional salinity gradient, while not critical for the mode mechanism, is still important for the oscillation period. The damping of the eigenmodes, according to the idealized model, is determined by horizontal diffusion. Consequently, the least-damped mode is the one with the smallest wave number and the greatest horizontal spatial scale. Other modes have shorter decay timescales, so that asymptotically at long time only the large-scale interdecadal mode survives in the system.

The eigenmode described in our study can explain the westward propagation of temperature anomalies on decadal timescales as detected in observations (*e.g.* Kushnir, 1994) as well as other properties of interdecadal variability highlighted in previous studies with comprehensive, intermediate-complexity, and simple climate models. For example, te Raa and Dijkstra (2002) discussed an oscillation that involved both meridional and Zonal Overturning Circulations (ZOC) in the Atlantic. In our model the phase of the oscillation associated with the AMOC intensification corresponds to the thermocline shoaling in the West and deepening in the East, which is a signature of a strengthening of the ZOC.

Another examples include explanations of AMOC variability that involve modifications of the subpolar or subtropical gyres and the upper ocean heat content in the northern Atlantic (*e.g.* Dong and Sutton, 2005; D'Orgeville and Peltier, 2009; Danabasoglu, 2008; Cheng et al., 2004). In our model both gyres are affected by anomalous currents associated with large-scale temperature anomalies (Fig. 3) and hence anomalies in the upper ocean heat content. Whereas the greatest changes in the gyre circulations occur when the total heat content in the upper northern Atlantic is either maximal or minimum, AMOC anomalies are strongest when heat content anomalies are weak (Fig. 2). These results imply that our interdecadal eigenmode is not only characteristic of the particular GCM we use, but can also account for previously noted features of interdecadal variability in other ocean and climate models.

To better understand the properties of the system we have also examined the biorthogonal of the leading eigenmode (*i.e.*, the least-damped eigenmode of the adjoint model). This "adjoint" mode describes the sensitivity of the leading "forward" mode; that is, it shows which regions of the ocean and which variables (temperature or salinity) should be perturbed to excite the forward mode. In other words, the adjoint mode is more relevant for perturbing the system, while the forward mode is more important in the asymptotic limit of long time.

Because the system is non-normal, the structure of the adjoint mode (the biorthogonal) is dramatically different from that of the forward mode. For example, temperature and

salinity have opposite effects on density in the eigenmode but constructive in the adjoint mode. The forward mode has the greatest signature in the upper ocean but the adjoint mode is more prominent in the deep ocean (where the mean flow and mean temperature and salinity gradients are minimum). These differences imply that standard statistical analyses used for studying AMOC variations may have difficulties in elucidating the properties of the leading eigenmode of the system since asymptotic characteristics of interdecadal variability can differ from those obtained from assessing short-term correlations.

As outlined by the idealized model, the nonnormality of the system is related to several factors leading to asymmetry in the linear prognostic equations. These factors include a significantly stronger stratification in the upper ocean than in the deep ocean, and the competition between the meridional gradients of temperature and of salinity in setting the meridional density gradient in the North Atlantic.

Several questions have not been yet addressed by this work. Even though the nonnormal properties of the oscillatory mode have been highlighted, we have not explored how atmospheric noise can excite this mode. As suggested by Ioannou (1995), the nonnormality should enhance the response of the AMOC to external perturbations. Another question is the robustness of the mode to changes in the surface boundary conditions. A new set of experiments (not shown) reveals that the mode can still exist for different boundary conditions (temperature restoring instead of constant heat fluxes). As expected, the eigenmode becomes more damped but retains its major properties, including the same oscillation period. Also, the sensitivity of the oscillatory mode to surface salinity perturbations becomes enhanced relatively to temperature perturbations (Sévellec and Fedorov, 2011). This latter property could be crucial for sustaining the mode by atmospheric synoptic noise.

Another issue not addressed in this study is the role of mesoscale eddies. In ocean models such as the one we use, turbulent mixing is represented by Gent-McWilliams eddy fluxes (Gent and McWilliams, 1990) and by diapycnal and isopycnal diffusion. This implies that

mesoscale eddies (Chelton et al., 2007) as well as the low-frequency variability associated with the eddying ocean dynamics (e.g. Berloff and McWilliams, 1999) are missing in our model. Given typical spatial scales of these eddies ($\sim$100 km), naturally they are filtered out from spatially integrated temperature indices such as the AMO index for example (SSTs averaged over the North Atlantic). However, they should be considered in future work as a potential source of oceanic internal noise and a possible contributor to low-frequency variability.

Another important issue is the effect of ocean-atmosphere interactions on the interdecadal mode. In particular, a series of studies have shown the importance of the thermal feedback on wind stress for generating (Cessi, 2000; Gallego and Cessi, 2000) and sustaining (Cessi and Paparella, 2001) decadal variability. Preliminary results from the IPSL coupled climate model (a model that has OPA as its oceanic component) reveal a robust 20-year interdecadal variability of the AMOC with dynamics apparently similar to those discussed in this study (Juliette Mignot, personal communication). Atlantic ocean variability in a coupled model with a simplified atmosphere and idealized continental geometry (John Marshall, personal communication) also resembles our mode. The nonnormal excitation of the interdecadal mode (Sévellec and Fedorov, 2011) and the role of coupled feedbacks are among the topics of ongoing and future work.

Acknowledgments. This research was supported by grants from NSF (OCE-0901921), DOE Office of Science (DE-FG02-08ER64590), and the David and Lucile Packard Foundation. FS thanks T. Huck and A. Colin de Verdière for useful comments on an early version of the manuscript. AVF thanks Peter Rhines and Igor Kamenkovich for a helpful discussion.

Appendix A: Idealized model incorporating the deep ocean

In this appendix we describe modifications of eqs (15a, b) necessary to include the effect of the deep ocean.

We first rename the Fourier amplitudes for temperature at the upper level as T^u_{cn} and T^u_{sn} and introduce two new dynamical variables T^d_{cn} and T^d_{sn} for the deep ocean. We neglect the meridional temperature gradient or mean velocity in the deep ocean because they are very weak as compared to those at the surface. We also ignore bottom topography and assume that the deep ocean temperature can be affected only by diffusion. It will be critical, however, that temperature anomalies in the deep ocean can change vertical shear in the ocean (because of thermal wind balance) and modify currents and hence temperature in the upper ocean. This effect will be included in the equations for T^u_{cn} and T^u_{sn}.

The aforementioned assumptions lead to a new system of equations:

$$\partial_t \begin{pmatrix} T^u_{cn} \\ T^u_{sn} \\ T^d_{cn} \\ T^d_{sn} \end{pmatrix} = \begin{pmatrix} -\kappa\left(\frac{n\pi}{W}\right)^2 & \frac{n\pi}{W}c & 0 & \frac{n\pi}{W}\left(\hat{u}+c_{\mathrm{Ro}}\right) \\ -\frac{n\pi}{W}c & -\kappa\left(\frac{n\pi}{W}\right)^2 & -\frac{n\pi}{W}\left(\hat{u}+c_{\mathrm{Ro}}\right) & 0 \\ 0 & 0 & -\kappa\left(\frac{n\pi}{W}\right)^2 & 0 \\ 0 & 0 & 0 & -\kappa\left(\frac{n\pi}{W}\right)^2 \end{pmatrix} \begin{pmatrix} T^u_{cn} \\ T^u_{sn} \\ T^d_{cn} \\ T^d_{sn} \end{pmatrix}, \tag{19}$$

where still $c{=}\overline{u}{+}\hat{u}{+}c_{\mathrm{Ro}}$, with $\hat{u}{=}\frac{\alpha g\tilde{h}}{f}\partial_y\overline{T}$ and $c_{\mathrm{Ro}}{=}\frac{\alpha g\tilde{h}h\beta_f}{f^2}\partial_z\overline{T}$.

A linear stability analysis yields four eigenvalues

$$\lambda_{1,2} = -\kappa\left(\frac{n\pi}{W}\right)^2 \pm i\frac{n\pi}{W}c, \quad \text{and} \quad \lambda_{3,4} = -\kappa\left(\frac{n\pi}{W}\right)^2, \tag{20}$$

corresponding to four eigenvectors

$$\langle \boldsymbol{u}_{1,2}| = (2c)^{-\frac{1}{2}}\left(\pm i, 1, 0, 0\right), \tag{21a}$$

$$\langle \boldsymbol{u}_3| = c^{-\frac{1}{2}}\left(\hat{u}+c_{\mathrm{Ro}}, 0, c, 0\right), \quad \text{and} \quad \langle \boldsymbol{u}_4| = c^{-\frac{1}{2}}\left(0, \hat{u}+c_{\mathrm{Ro}}, 0, c\right). \tag{21b}$$

The corresponding biorthogonal vectors are

$$\langle \boldsymbol{u}^\dagger_{1,2}| = (2c)^{-\frac{1}{2}}\left[\pm ic, c, \pm i\left(\hat{u}+c_{\mathrm{Ro}}\right), \hat{u}+c_{\mathrm{Ro}}\right], \tag{22a}$$

$$\langle \boldsymbol{u}^\dagger_3| = c^{-\frac{1}{2}}\left(0, 0, 1, 0\right), \quad \text{and} \quad \langle \boldsymbol{u}^\dagger_4| = c^{-\frac{1}{2}}\left(0, 0, 0, 1\right). \tag{22b}$$

Appendix B: Idealized model with salinity

In this appendix we derive a new set of equations for the idealized model, similar to eqs (15a,b), but with salinity variations included. We first introduce S_{cn} and S_{sn} - the Fourier amplitudes for the upper-ocean salinity (similar to T_{cn} and T_{sn}). Using a linear equation of state for seawater, we obtain:

$$\partial_t \begin{pmatrix} T_{cn} \\ T_{sn} \\ S_{cn} \\ S_{sn} \end{pmatrix} = \begin{pmatrix} -\kappa\left(\frac{n\pi}{W}\right)^2 & A_{1,2} & 0 & A_{1,4} \\ A_{2,1} & -\kappa\left(\frac{n\pi}{W}\right)^2 & A_{2,3} & 0 \\ 0 & A_{3,2} & -\kappa\left(\frac{n\pi}{W}\right)^2 & A_{3,4} \\ A_{4,1} & 0 & A_{4,3} & -\kappa\left(\frac{n\pi}{W}\right)^2 \end{pmatrix} \begin{pmatrix} T_{cn} \\ T_{sn} \\ S_{cn} \\ S_{sn} \end{pmatrix}, \tag{23}$$

with

$$\begin{aligned} A_{1,2} = -A_{2,1} &= \frac{n\pi}{W}\left(\frac{\alpha g\tilde{h}}{f}\partial_y\overline{T} + \frac{\alpha g\tilde{h}h\beta_f}{f^2}\partial_z\overline{T} + \overline{u}\right), \\ A_{2,3} = -A_{1,4} &= \frac{n\pi}{W}\left(\frac{\beta g\tilde{h}}{f}\partial_y\overline{T} + \frac{\beta g\tilde{h}h\beta_f}{f^2}\partial_z\overline{T}\right), \\ A_{3,2} = -A_{4,1} &= \frac{n\pi}{W}\left(\frac{\alpha g\tilde{h}}{f}\partial_y\overline{S} + \frac{\alpha g\tilde{h}h\beta_f}{f^2}\partial_z\overline{S}\right), \\ A_{4,3} = -A_{3,4} &= \frac{n\pi}{W}\left(\frac{\beta g\tilde{h}}{f}\partial_y\overline{S} + \frac{\beta g\tilde{h}h\beta_f}{f^2}\partial_z\overline{S} - \overline{u}\right), \end{aligned}$$

where $\partial_y\overline{S}$ and $\partial_z\overline{S}$ are the background meridional and vertical gradients of salinity, and β is the haline contraction coefficient.

The eigenvalues of this system are

$$\lambda_{1,2} = -\kappa\left(\frac{n\pi}{W}\right)^2 \pm i\frac{n\pi}{W}c, \text{ and } \lambda_{3,4} = -\kappa\left(\frac{n\pi}{W}\right)^2 \pm i\frac{n\pi}{W}\overline{u}, \tag{24}$$

with the corresponding eigenvectors

$$|\boldsymbol{u}_{1,2}\rangle = \left[2\left(\hat{u} + c_{\mathrm{Ro}}\right)\right]^{-\frac{1}{2}} \begin{pmatrix} \mp i\left(\frac{g\tilde{h}}{f}\partial_y\overline{T} + \frac{g\tilde{h}h\beta_f}{f^2}\partial_z\overline{T}\right) \\ \frac{g\tilde{h}}{f}\partial_y\overline{T} + \frac{g\tilde{h}h\beta_f}{f^2}\partial_z\overline{T} \\ \mp i\left(\frac{g\tilde{h}}{f}\partial_y\overline{S} + \frac{g\tilde{h}h\beta_f}{f^2}\partial_z\overline{S}\right) \\ \frac{g\tilde{h}}{f}\partial_y\overline{S} + \frac{g\tilde{h}h\beta_f}{f^2}\partial_z\overline{S} \end{pmatrix}, \tag{25a}$$

and

$$\langle \boldsymbol{u}_{3,4}| = \left[2\left(\hat{u}+c_{\mathrm{Ro}}\right)\right]^{\frac{1}{2}}\left(\pm i\beta,\beta,\pm i\alpha,\alpha\right). \tag{25b}$$

The corresponding biorthogonal vectors are

$$|\boldsymbol{u}^{\dagger}_{1,2}\rangle = \left[2\left(\hat{u}+c_{\mathrm{Ro}}\right)\right]^{-\frac{1}{2}}\left(\mp i\alpha,-\alpha,\pm i\beta,\beta\right), \tag{26a}$$

and

$$|\boldsymbol{u}^{\dagger}_{3,4}\rangle = \left[2\left(\hat{u}+c_{\mathrm{Ro}}\right)\right]^{\frac{1}{2}}\begin{pmatrix} \pm i\left(\frac{g\tilde{h}}{f}\partial_y\overline{S}+\frac{g\tilde{h}h\beta_f}{f^2}\partial_z\overline{S}\right) \\ -\frac{g\tilde{h}}{f}\partial_y\overline{S}-\frac{g\tilde{h}h\beta_f}{f^2}\partial_z\overline{S} \\ \mp i\left(\frac{g\tilde{h}}{f}\partial_y\overline{T}+\frac{g\tilde{h}h\beta_f}{f^2}\partial_z\overline{T}\right) \\ \frac{g\tilde{h}}{f}\partial_y\overline{T}+\frac{g\tilde{h}h\beta_f}{f^2}\partial_z\overline{T} \end{pmatrix}. \tag{26b}$$

References

Arzel, O., T. Huck, and A. Colin de Verdière, 2006: The different nature of the interdecadal variability of the thermohaline circulation under mixed and flux boundary conditions. *J. Phys. Oceanogr.*, **36**, 1703–1718.

Berloff, P. S. and J. C. McWilliams, 1999: Large-scale low-frequency variability in wind-driven ocean gyres. *J. Phys. Oceanogr.*, **29**, 1925–1949.

Blanke, B. and P. Delecluse, 1993: Variability of the tropical Atlantic ocean simulated by a general circulation model with two different mixed-layer physics. *J. Phys. Oceanogr.*, **23**, 1363–1388.

Cessi, P., 2000: Thermal feedback on wind stress as a contributing cause of climate variability. *J. Climate*, **13**, 232–244.

Cessi, P. and F. Paparella, 2001: Excitation of basin modes by ocean-atmosphere coupling. *Geophys. Res. Lett.*, **28**, 2437–2440.

Chelton, D. B., et al., 2007: Global observations of large oceanic eddies. *Geophys. Res. Lett.*, **34**, L15 606.

Chen, F. and M. Ghil, 1995: Interdecadal variability of the thermohaline circulation and high-latitude surface flux. *J. Phys. Oceanogr.*, **25**, 2547–2568.

Cheng, W., R. Bleck, and C. Rooth, 2004: Multi-decadal thermohaline variability in an ocean-atmosphere general circulation model. *Clim. Dyn.*, **22**, 573–590.

Colin de Verdière, A., 1988: Buoyancy driven planetary flow. *J. Mar. Res.*, **46**, 215–265.

Colin de Verdière, A. and T. Huck, 1999: Baroclinic instability: an oceanic wavemaker for interdecadal variability. *J. Phys. Oceanogr.*, **29**, 893–910.

Danabasoglu, G., 2008: On multidecadal variability of the Atlantic Meridional Overturning Circulation in the community climate system model version 3. *J. Climate*, **21**, 5524–5544.

Delworth, T. L. and M. E. Mann, 2000: Observed and simulated multidecadal variability in the northern hemisphere. *Clim. Dyn.*, **16**, 661–676.

Dijkstra, H. A., et al., 2006: On the physics of the Atlantic Multidecadal Oscillation. *Ocean Dyn.*, **56**, 36–50.

Dong, B. and R. T. Sutton, 2005: Mechanism of interdecadal thermohaline circulation variability in a coupled ocean-atmosphere GCM. *J. Climate*, **18**, 1117–1135.

D'Orgeville, M. and W. R. Peltier, 2009: Implications of both statistical equilibrium and global warming simulations with CCSM3. Part II: On the multidecadal variability in the North Atlantic basin. *J. Climate*, **22**, 5298–5318.

Farrell, B. F. and P. J. Ioannou, 1996: Generalized stability theory. Part I: autonomous operators. *J. Atmos. Sci.*, **35**, 2025–2040.

Frankcombe, L. M. and Dijkstra, 2009: Coherent multidecadal variability in North Atlantic sea level. *Geophys. Res. Lett.*, **36**, L15 604.

Frankcombe, L. M., H. A. Dijkstra, and A. von der Heydt, 2008: Sub-surface signatures of the Atlantic Multidecadal Oscillation. *Geophys. Res. Lett.*, **35**, L19 602.

—, 2009: Noise-Induced Multidecadal Variability in the North Atlantic: Excitation of Normal Modes. *J. Phys. Oceanogr.*, **39**, 220–233.

Gallego, B. and P. Cessi, 2000: Exchange of heat and momentum between the atmosphere and the ocean: a minimal model of decadal oscillations. *Clim. Dyn.*, **16**, 479–489.

Ganachaud, A. and C. Wunsch, 2000: Improved estimates of global ocean circulation, heat transport and mixing from hydrographic data. *Nature*, **408**, 453–457.

Gent, P. R. and J. C. McWilliams, 1990: Isopycnal mixing in ocean circulation model. *J. Phys. Oceanogr.*, **20**, 150–155.

Goldenberg, S. B., C. W. Landsea, and W. M. Mestas-Nuñez, A. M. andGray, 2001: The Recent Increase in Atlantic Hurricane Activity: Causes and Implications. *Nature*, **293**, 474–479.

Held, I. M., 1983: *Stationary and quasi-stationary eddies in the extratropical troposphere: Theory*. Large-Scale Dynamical Processes in the Atmosphere, B. J. Hoskins, and R. P. Pearce, Eds., Academic Press, pp. 127–168.

Huck, T., A. Colin de Verdière, and A. J. Weaver, 1999: Interdecadal variability of the thermohaline circulation in box-ocean models forced by fixed surface fluxes. *J. Phys. Oceanogr.*, **29**, 865–892.

Huck, T. and G. K. Vallis, 2001: Linear stability analysis of three-dimensional thermally-driven ocean circulation : application to interdecadal oscillations. *J. Climate*, **53A**, 526–545.

Ioannou, P. J., 1995: Nonnormality increases variance. *J. Atmos. Sci.*, **52**, 1155–1158.

IPCC, 2007: *Climate Change 2007 - The Physical Science Basis: Contribution of Working Group I to the Fourth Assessment Report of the IPCC*. Cambridge: Cambridge University Press.

Killworth, P. D., D. B. Chelton, and R. A. de Szoeke, 1997: The speed of observed and theoretical long extratropical planetary waves. *J. Phys. Oceanogr.*, **27**, 1946–1966.

Knight, J. R., et al., 2005: A signature of persistent natural thermohaline circulation cycles in observed climate. *Geophys. Res. Lett.*, **32**, L20 708.

Kushnir, Y., 1994: Interdecadal variations in North Atlantic sea surface temperature and associated atmospheric conditions. *J. Climate*, **7**, 141–157.

Latif, M., 1997: Dynamics of interdecadal variability in coupled ocean-atmosphere models. *J. Climate*, **11**, 602–624.

Madec, G., et al., 1998: OPA 8.1 Ocean General Circulation Model reference manual. Tech. rep., Institut Pierre-Simon Laplace (IPSL), France, No11, 91pp.

Redi, M. H., 1982: Oceanic isopycnalmixing by coordinate rotation. *J. Phys. Oceanogr.*, **12**, 1154–1158.

Rossby, C. G. et al., 1939: Relation between variations in the intensity of the zonal circulation of the atmosphere and the displacements of the semi-permanent centers of action. *J. Mar. Res.*, **2**, 38–55.

Sévellec, F. and A. V. Fedorov, 2011: Optimal surface temperature and salinity perturbations for the Atlantic meridional overturning circulation. *J. Phys. Oceanogr.*, submitted.

Sévellec, F., et al., 2009: Non-normal multidecadal response of the thermohaline circulation induced by optimal surface salinity perturbations. *J. Phys. Oceanogr.*, **39**, 852–872.

Strogatz, S. H., 1994: *Nonlinear dynamics and chaos with applications to physics, biology, chemistry and engineering*. Advanced book program, Perseus book, 498pp pp.

Sutton, R. W. and D. L. R. Hodson, 2003: Influence of the ocean on North Atlantic climate variability 1671-1999. *J. Climate*, **16**, 3296–3313.

—, 2005: Atlantic ocean forcing of North American and European summer climate. *Science*, **309**, 115–118.

Talley, L. D., J. L. Reid, and P. E. Robbins, 2003: Data-based meridional overturning streamfunctions for the global ocean. *J. Climate*, **16**, 3213–3226.

te Raa, L. A. and H. A. Dijkstra, 2002: Instability of the thermohaline ocean circulation on interdecadal timescales. *J. Phys. Oceanogr.*, **32**, 138–160.

—, 2003: Sensitivity of North Atlantic Multidecadal Variability to Freshwater Flux Forcing. *J. Climate*, **16**, 2586–2601.

te Raa, L. A., J. Gerrits, and H. A. Dijkstra, 2004: Identification of the Mechanism of Interdecadal Variability in the North Atlantic Ocean. *J. Phys. Oceanogr.*, **34**, 2792–2807.

Weaver, A. T., J. Vialard, and D. L. T. Anderson, 2003: Three- and four-dimensional variational assimilation with a general circulation model of the tropical Pacific Ocean. Part 1: formulation, internal diagnostics and consistency checks. *Mon. Wea. Rev.*, **131**, 1360–1378.

Yoshimori, M., et al., 2010: Simulated decadal oscillations of the atlantic meridional overturning circulation in a cold climate state. *Clim. Dyn.*, **34**, 101–121.

List of Figures

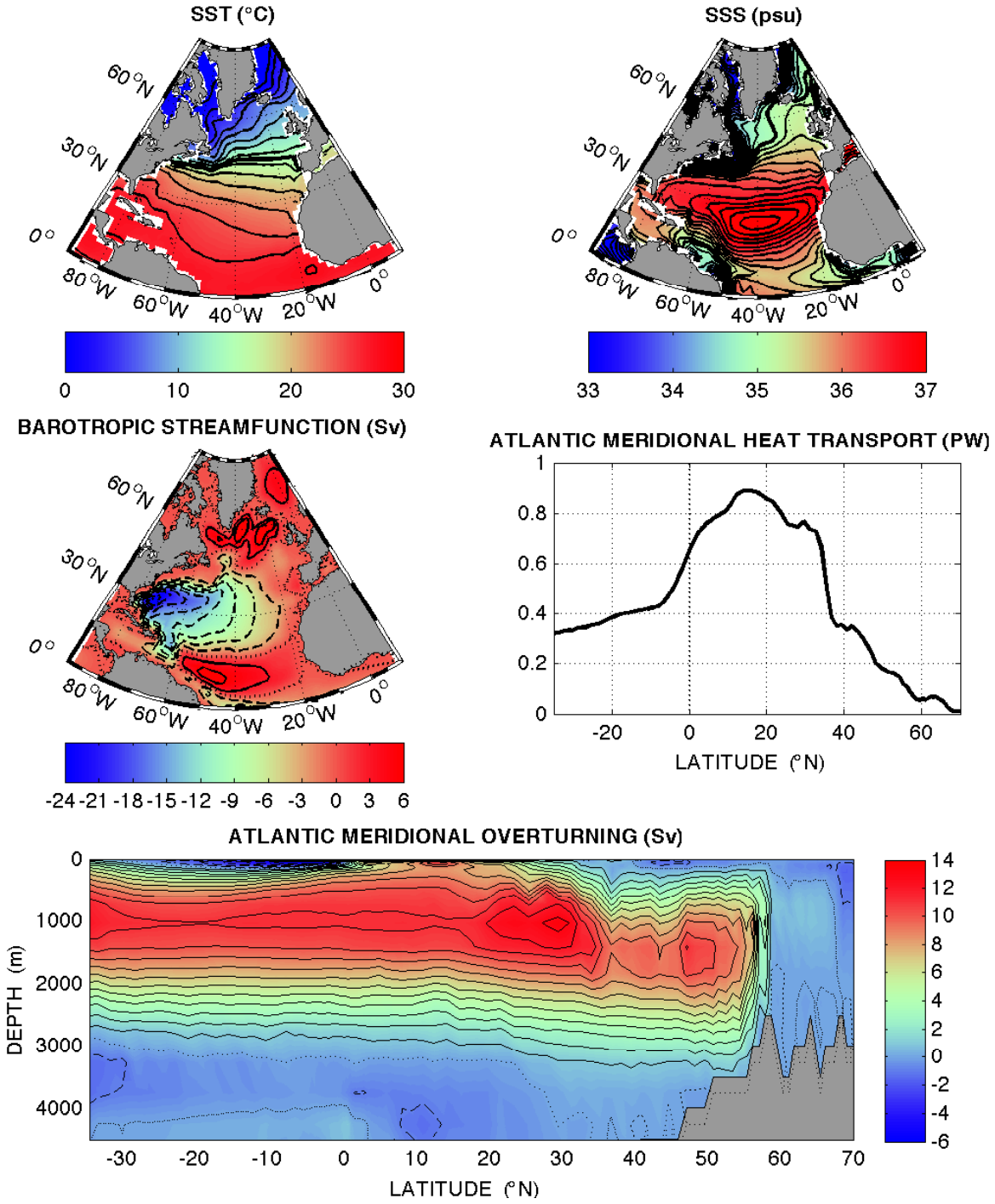

FIGURE 1: The climatological basic state of the Atlantic ocean as reproduced by the full GCM. (Top left) Sea surface temperature; contour intervals (CI) are 2°C, the heavy line corresponds to 20°C. (Top right) Sea surface salinity; CI are 0.2 psu, the heavy line corresponds to 35 psu. (Middle left) Barotropic streamfunction; CI are 3 Sv. (Middle right) The ocean meridional heat transport as a function of latitude. (Bottom) Zonally-averaged streamfunction for the Atlantic meridional overturning circulation; CI are 1 Sv. In the two plots of streamfunction, plain, dashed and dotted lines indicate positive, negative and zero values.

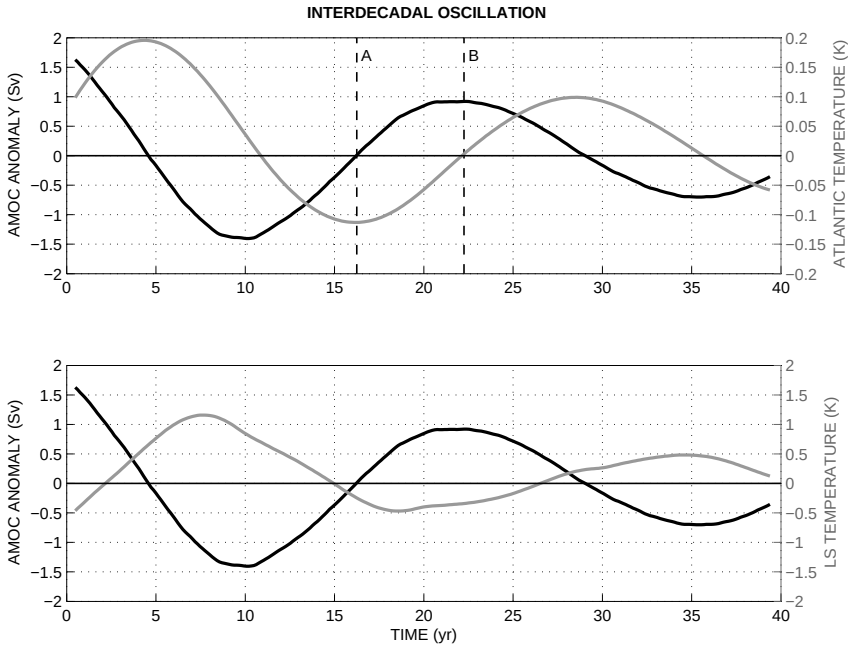

FIGURE 2: Temporal evolution of the least-damped eigenmode of the tangent linear model. (Top) Variations in the AMOC volume transport (black line) and temperature in the northern Atlantic (gray line). The AMOC streamfunction is evaluated between 0-1200 m, 34-62°N; temperature is averaged over the total depth of the ocean between 34-62°N and 85°W-12°E. (Bottom) Variations in the AMOC volume transport (black line) and the Labrador Sea temperature (grey line, LS). The vertical dashed lines labeled A and B denote two phases of the oscillation. The spatial structure of the mode for the two phases is shown in Figs. 3 and 4.

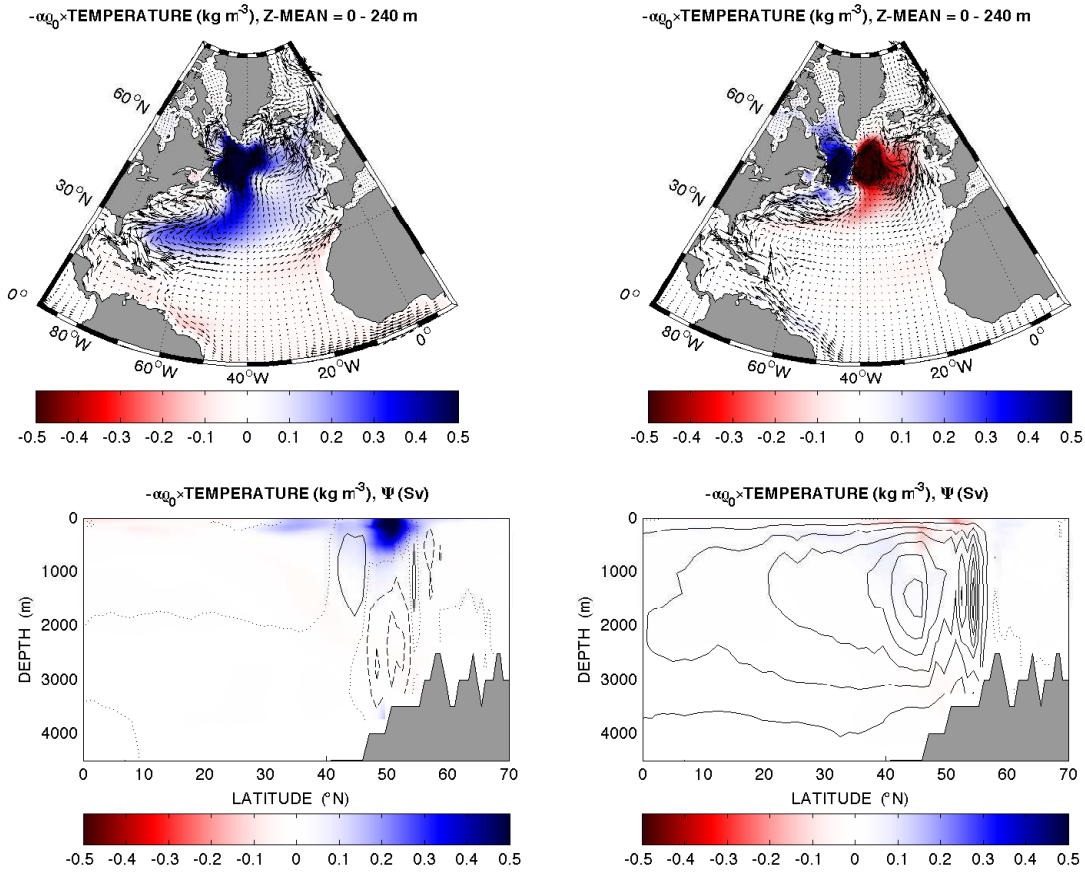

FIGURE 3: The spatial structure of the least-damped eigenmode of the tangent linear mode: anomalies of (top) upper-ocean temperature and surface currents and of (bottom) meridional streamfuction and zonally-averaged temperature for phases A and B of the oscillation. During phase A (left) there exists a strong temperature anomaly in the northern Atlantic with a nonzero zonal mean, but the AMOC overturning anomaly is nearly zero. During phase B (right) there develops a dipole-like temperature anomaly (with a zero zonal mean), associated with a strong AMOC anomaly. The two instances (A and B) are separated by a quarter-phase or roughly 6 years. Temperature is given in terms of density. The upper-ocean temperature is averaged over the top 240 m. For the streamfunction plot: plain, dashed and dotted lines indicate positive, negative and zero values, respectively; contour intervals are 1 Sv. Current velocities reach 6 cm s^{-1}. Note that all variables can be multiplied by an arbitrary factor since we consider a linear problem.

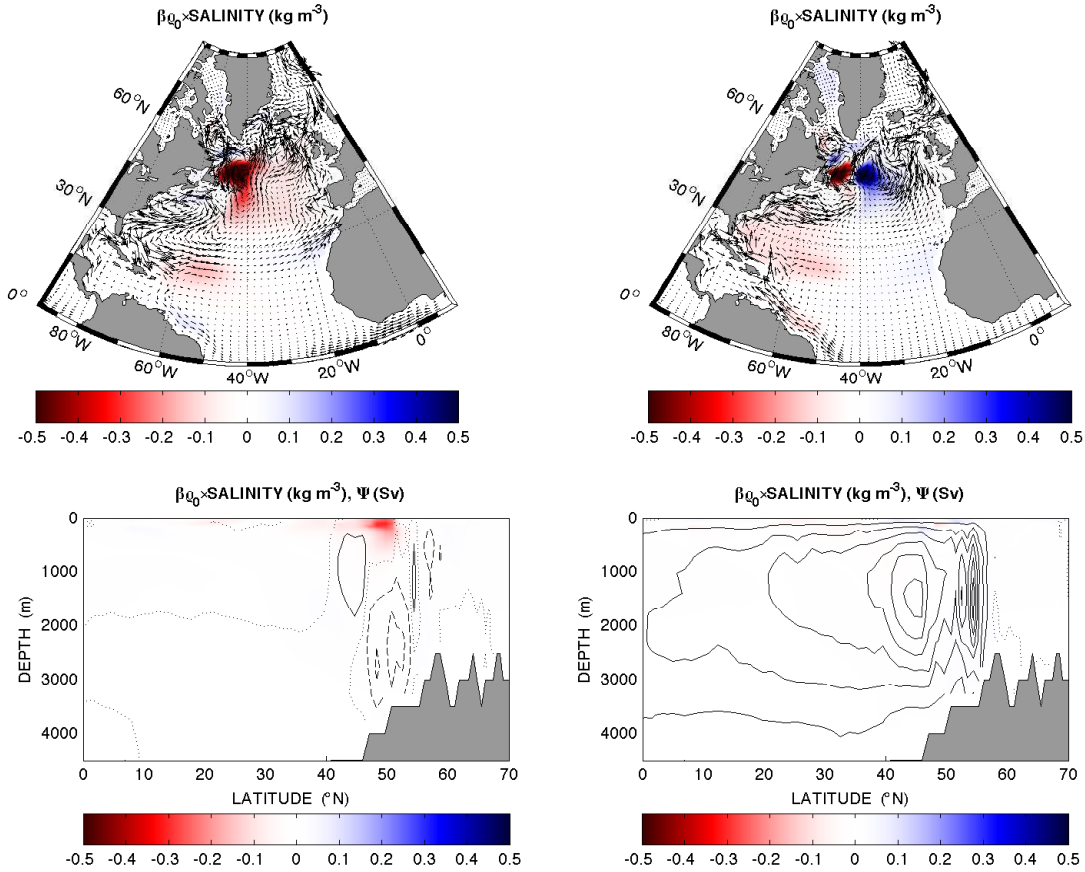

FIGURE 4: As in Fig. 3 but for salinity variations.

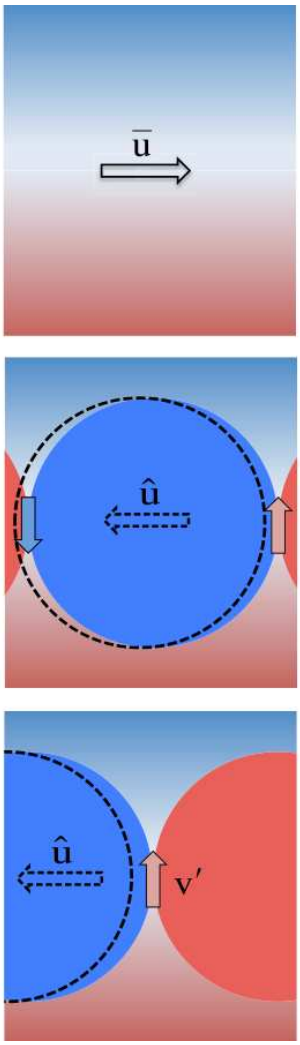

FIGURE 5: A schematic of the least-damped eigenmode with the mechanism of the westward propagation of temperature anomalies. Blue and red represent the mean temperature distribution (light colors) and the temperature anomalies in the upper ocean (heavier colors), respectively. (Top) The background meridional temperature gradient and the corresponding eastward geostrophic flow $\overline{u}$. (Middle) Phase A of the oscillation with a strong cold temperature anomaly but no change in the meridional overturning. (Bottom) Phase B of the oscillation with a dipole temperature anomaly and a strong anomaly in the overturning associated with the anomalous meridional geostrophic flow v'. The cold temperature anomaly in the middle panel induces cyclonic circulation in the ocean that transports cold water southward along the western flank of the anomaly and warm water northward along the eastern flank. This water transport results in the westward propagation of the original temperature anomaly with the equivalent velocity $\hat{u}$ (geostrophic self-advection). The net of two velocities $(\hat{u}+\overline{u})$ is westward, as long as $|\hat{u}|>|\overline{u}|$. The β-effect contributes to the westward propagation as well.

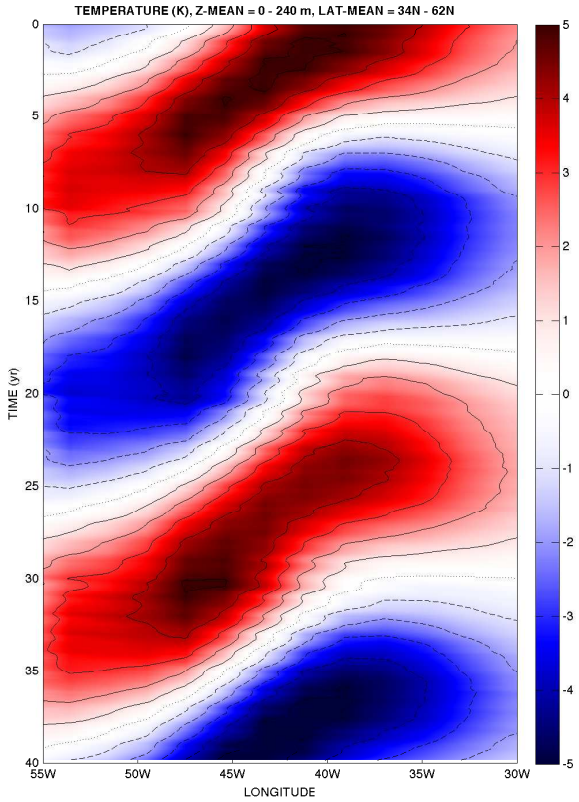

FIGURE 6: A Hovmöller diagram showing westward propagation of temperature anomalies in the least-damped eigenmode. Temperature has been averaged over the upper 240 m meters in the latitudinal band 34°N to 62°N. Contour intervals are 1°C.

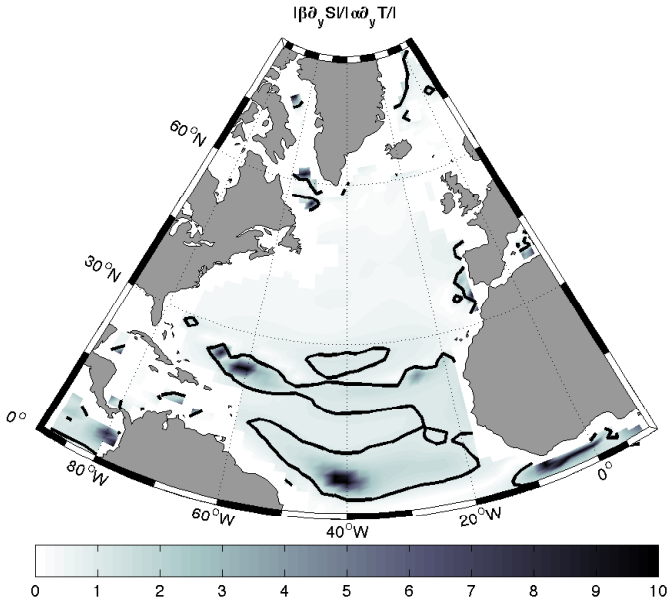

FIGURE 7: Density ratio between the meridional gradients of salinity and temperature averaged in the upper 500 m for the mean state produced by the full ocean GCM ($|\beta\partial_y\overline{S}|/|\alpha\partial_y\overline{T}|$). The contour line corresponds to the ratio of 1.

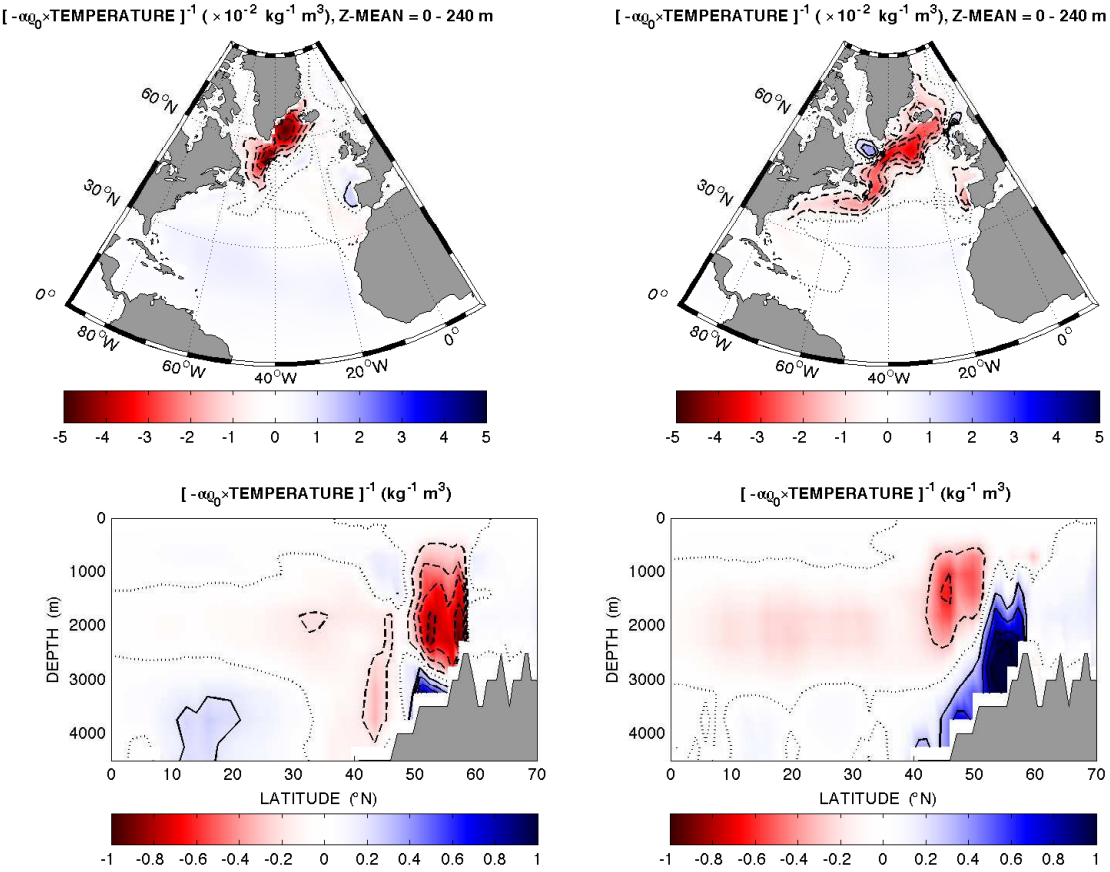

FIGURE 8: As in Fig. 3 but for the least-damped eigenmode of the adjoint model. Horizontal velocities and the meridional streamfunction are not shown.

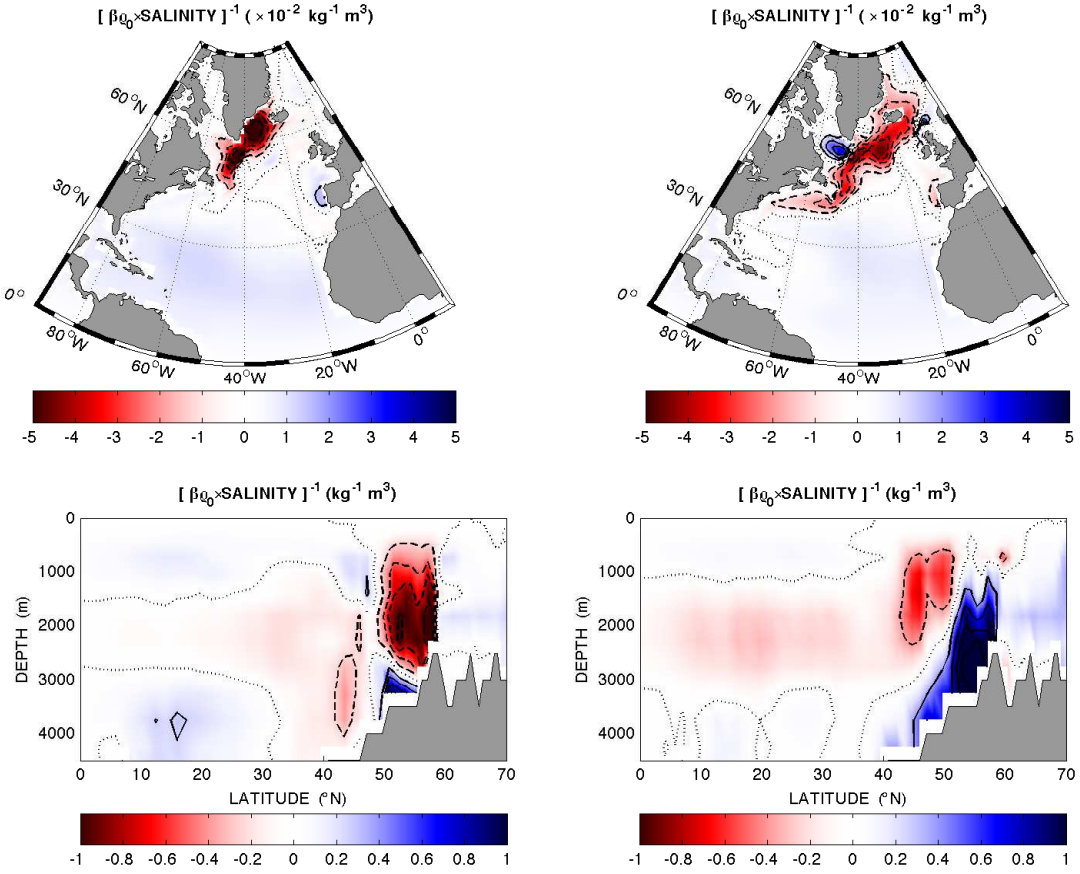

FIGURE 9: As in Fig. 8 but for the salinity component of the least-damped eigenmode of the adjoint model.

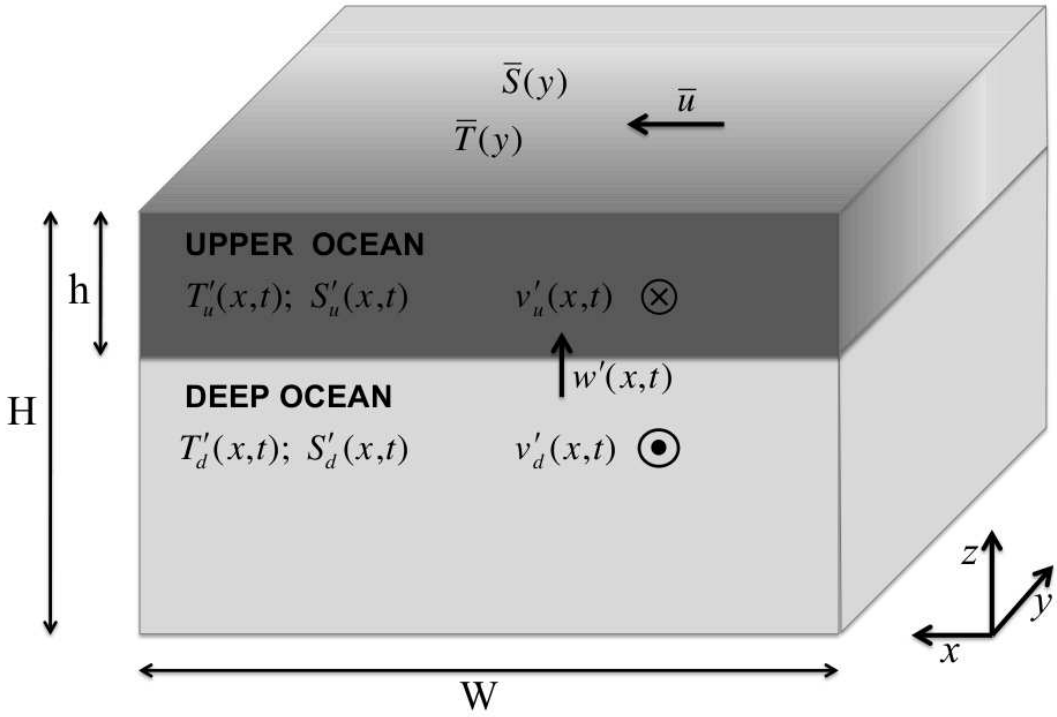

FIGURE 10: A schematic of the idealized model. The two levels of the model represent the upper and deep ocean, respectively. The model four prognostic variables are temperature and salinity in the upper and deep ocean (T'_u, S'_u, T'_d, and S'_d, respectively). The three diagnostic variables are meridional velocities in the upper and deep ocean (v'_u and v'_d, respectively), and the vertical velocity between the two levels (w'). The main model parameters are the upper ocean thickness (h), the total ocean depth (H), the zonal extent of the Atlantic basin (W), and the mean meridional flow ($\overline{u}$) and temperature and salinity fields in the upper ocean ($\overline{T}$ and $\overline{S}$, respectively). The intensity of the shading (lighter to darker) represents the value of the mean temperature and salinity (cooler to warmer and fresher to saltier). In the upper ocean, we use a linear functions of y. In the deep ocean, we use a constant values equal to the value at the southern basin boundary of the upper ocean. The dependency of the model variables from space coordinates (zonal - x, meridional - y, and vertical - z) and time (t) is shown in brackets.

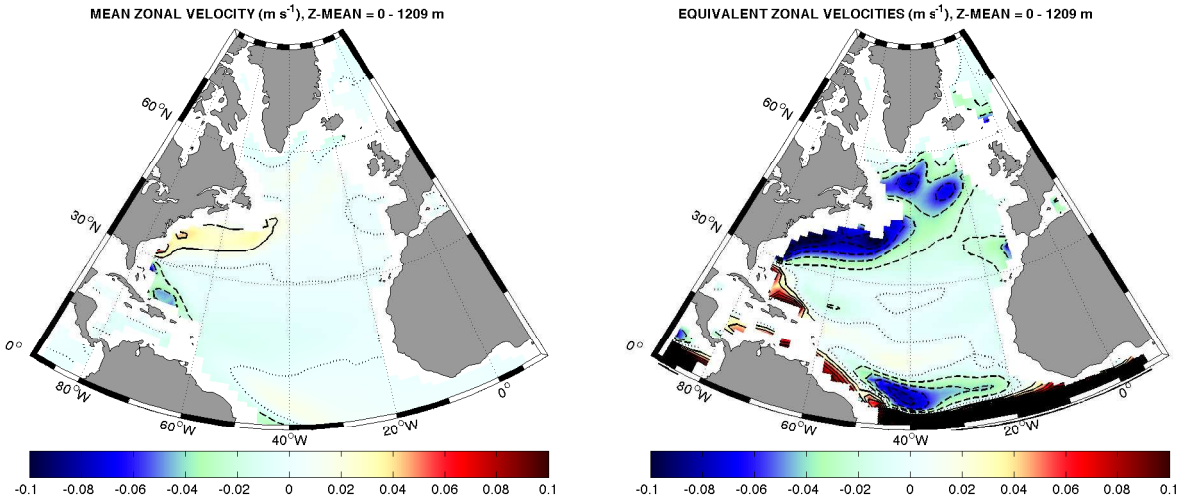

FIGURE 11: (Left) Mean zonal velocity in the upper ocean. (Right) Equivalent zonal velocity in the upper ocean calculated as $g\tilde{h}(\alpha\partial_y\overline{T} - \beta\partial_y\overline{S})/f$. The β-effect also contributes to westward propagation. The fields are produced by the full ocean GCM.

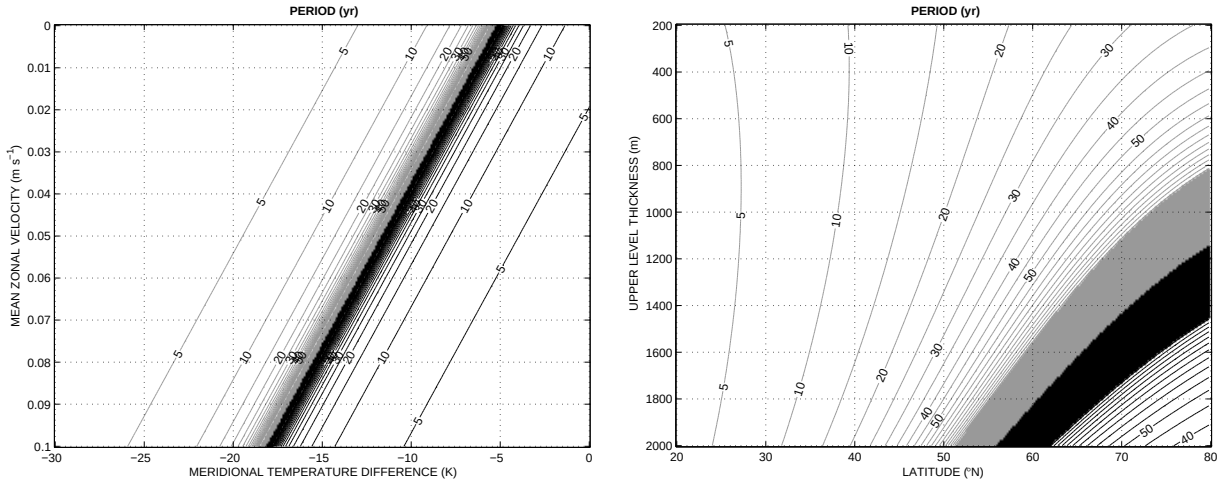

FIGURE 12: The period of the interdecadal mode in the idealized model, obtained from expression (18) with n=1. Contour intervals are 5 yr, black and grey lines indicate eastward and westward propagation, respectively. Along the boundary between black and grey lines the period is infinite.

List of Tables

TABLE 1: Typical parameters used in the idealized model.

h	1200 m	upper level thickness
H	3500 m	total ocean depth
W	60°	zonal basin size
L	60°	meridional basin size
κ	2×10^{3} m^{2} s^{-1}	horizontal tracer diffusivity
g	9.8 m s^{-2}	acceleration due to gravity
f	10^{-4} s^{-1}	Coriolis parameter
β_f	7.5×10^{-12} m^{-1} s^{-1}	β-effect (the gradient of planetary vorticity)
α	2×10^{-4} K^{-1}	thermal expansion coefficient
β	7×10^{-4} psu^{-1}	haline contraction coefficient
ΔT	–15 K	mean meridional temperature contrast
ΔS	–1.5 psu	mean meridional salinity contrast
$\overline{u}$	$+2.5\times10^{-2}$ m s^{-1}	mean zonal in the upper ocean

TABLE 2: The period and e-folding decay time scale of the interdecadal oscillation obtained from expression (18) with n=1 for the idealized model with different combinations of the mean meridional salinity contrast and zonal velocity. Nonzero values are taken from Tab. 1.

Model		Period (Π)	decay (τ)
Tangent linear GCM		24.0 yr	–40.0 yr
Idealized models:	$\partial_{y/z}S$=0, $\overline{u}$=0	5.1 yr	–36.1 yr
	$\partial_{y/z}S$=0, $\overline{u}\neq$0	7.8 yr	–36.1 yr
	$\partial_{y/z}S\neq$0, $\overline{u}$=0	8.8 yr	–36.1 yr
	$\partial_{y/z}S\neq$0, $\overline{u}\neq$0	22.4 yr	–36.1 yr